

# Alpha-nucleus optical potentials from chiral EFT $NN$ interactions

V. Durant<sup>1,\*</sup> and P. Capel<sup>1,2,†</sup>

<sup>1</sup>*Institut für Kernphysik, Johannes Gutenberg-Universität Mainz, D-55099 Mainz, Germany*

<sup>2</sup>*Physique Nucléaire et Physique Quantique (CP 229),  
Université libre de Bruxelles (ULB), B-1050 Brussels, Belgium*

We present a determination of optical potentials for  $^4\text{He}$ -target collisions using the double-folding method based on chiral effective field theory nucleon-nucleon interactions at next-to-next-to-leading order combined with state-of-the-art nucleonic densities. The imaginary part of the optical potentials is obtained applying dispersion relations. With these potentials, we compute the elastic scattering of  $^4\text{He}$  off various targets, from  $^4\text{He}$  to  $^{120}\text{Sn}$ . We study the sensitivity of our predicted cross sections to the choice of nucleon-nucleon interactions and nuclear densities. Very good agreement is obtained with existing elastic-scattering data for  $^4\text{He}$  energies between 100 and 400 MeV without any fitting parameter.

## I. INTRODUCTION

The interaction between colliding nuclei constitutes a significant input in the modeling of nuclear reactions [1]. Given its complicated nature, the nuclear part of that interaction has typically been described by fitting parameters of phenomenological potentials, which rely on the existence of experimental data. Thus, they are accurate but lack predictive power. Recently, with the development of precise nucleon-nucleon ( $NN$ ) interactions, efforts have been made to derive such reaction potentials from first principles. For example, in Refs. [2–5], nucleon-nucleus optical potentials have been derived using chiral effective field theory (EFT) interactions as input.

For modern nuclear forces, chiral EFT has become the standard method for developing interactions rooted in the symmetries of quantum chromodynamics (see, e.g., Refs. [6–8] for reviews). Based on a power counting scheme,  $NN$  interactions can be expressed as an expansion that starts at leading order (LO), followed by contributions at next-to-leading order (NLO) and next-to-next-to leading order ( $N^2\text{LO}$ ), etc., which provides a systematic improvement of the description of observables.

In this work, we concentrate on the derivation of nucleus-nucleus potentials through the application of the double-folding model. This technique constitutes a first-order approximation to optical potentials derived from Feshbach's reaction theory [1]. In this formalism, it is possible to determine nucleus-nucleus interactions using more fundamental inputs: realistic nuclear densities and microscopic  $NN$  interactions. Interesting results have been obtained in such a way to determine the real part of the optical potentials [9, 10], or the real and imaginary parts using a  $G$ -matrix approach [11–13]. In our previous studies [14, 15], we have explored the possibility to describe the interaction between two colliding nuclei through the double folding of a  $NN$  interaction developed within a chiral EFT framework.

In Refs. [14, 15], we have studied the elastic scattering and low-energy fusion reactions of three systems:  $^{12}\text{C}$ - $^{12}\text{C}$ ,  $^{16}\text{O}$ - $^{16}\text{O}$ , and  $^{12}\text{C}$ - $^{16}\text{O}$ . To this end, we have derived optical potentials using the double-folding method with local chiral EFT potentials derived as in Refs. [16, 17]. We have used these  $NN$  interactions regulated in coordinate space with cutoffs  $R_0 = 1.2, 1.4$  and  $1.6$  fm, which were developed in Ref. [14], and adopted two-parameter Fermi parametrizations [9] or realistic density profiles from electron scattering [18] in the folding procedure. The choice of realistic densities gives significant improvement, leading to good agreement with existing data for a variety of collision observables. Elastic-scattering calculations are strongly sensitive to the choice of the imaginary part of the potential. To simulate this absorptive part, we have explored two possibilities: the first one being a zeroth-order approximation setting the imaginary part proportional to the real double-folding potential, as suggested in Ref. [10]. The second possibility is the use of dispersion relations between the real and imaginary parts of the interaction [19, 20]. While the former way provides acceptable results, but relies on a free parameter, the latter provides an efficient constraint on the imaginary term of the nucleus-nucleus interactions leading to much better agreement with the data without involving any free parameter. The use of these potentials gives excellent reproduction of elastic-scattering data at several energies for the collision of closed and non-closed shell nuclei [15].

To further test the validity of our approach, in this work we analyze elastic scattering involving the light nucleus  $^4\text{He}$ , which, due to its zero spin-isospin nature and large binding energy, plays a key role in nuclear reactions as well as nuclear astrophysics [21–23]. To this end, we start this study by analyzing the symmetric  $^4\text{He}$ - $^4\text{He}$  collision, which is a relatively simple system from which we can draw conclusions on the interaction. We then extend our study towards much heavier targets, up to  $^4\text{He}$ - $^{120}\text{Sn}$ . Due to the aforementioned interest of  $\alpha$  scattering, we have selected experimental data to explore collisions involving nuclei for which we have reliable density profiles. Accordingly, we show results for the elastic-scattering at intermediate energies of six different systems:  $^4\text{He}$ - $^4\text{He}$ ,

\* Email: vdurant@uni-mainz.de

† Email: pcapel@uni-mainz.de

$^4\text{He-}^{12}\text{C}$ ,  $^4\text{He-}^{16}\text{O}$ ,  $^4\text{He-}^{40}\text{Ca}$ ,  $^4\text{He-}^{48}\text{Ca}$ , and  $^4\text{He-}^{120}\text{Sn}$  and compare our results with experimental data [24–33]. In all cases, we test the sensitivity of elastic-scattering cross sections to the chosen  $NN$  interaction, the nuclear density, as well as the impact of the description of the imaginary part using dispersion relations.

This paper is organized as follows: in Sec. II we give a brief overview of the formalism of the double-folding technique and the ways of building the imaginary part of the optical potential. In Sec. III we present results for the  $^4\text{He-}^4\text{He}$  elastic scattering. We follow in Sec. IV with an analysis of results for heavier targets:  $^4\text{He-}^{12}\text{C}$ ,  $^4\text{He-}^{16}\text{O}$ ,  $^4\text{He-}^{40}\text{Ca}$ ,  $^4\text{He-}^{48}\text{Ca}$ , and  $^4\text{He-}^{120}\text{Sn}$ . Finally, we summarize and give an outlook in Sec. V.

## II. OPTICAL POTENTIALS

### A. Real part: double-folding formalism

The real part of the potential simulating the interaction between two nuclei can be obtained through a double-folding procedure [1, 34]. In this formalism, the nuclear part of the potential between nucleus 1—of atomic and mass numbers  $Z_1$  and  $A_1$ —and nucleus 2—of atomic and mass numbers  $Z_2$  and  $A_2$ —can be constructed from a  $NN$  interaction  $v$  by folding it over the nucleonic densities ( $\rho_1$  and  $\rho_2$ , respectively). In this section, we briefly present the formalism for the double-folding potentials that follows Refs. [11, 14]. The resulting antisymmetrized potential  $V_F$  is the sum of a direct (D) and an exchange (Ex) contributions:  $V_F = V_D + V_{\text{Ex}}$ . The direct part is the average of the  $NN$  interaction over both nucleonic densities and reads

$$V_D(r) = \sum_{i,j=n,p} \iint \rho_1^i(\mathbf{r}_1) v^{ij}(\mathbf{s}) \rho_2^j(\mathbf{r}_2) d^3\mathbf{r}_1 d^3\mathbf{r}_2, \quad (1)$$

where  $\mathbf{r}$  is the relative coordinate between the centers of mass of the nuclei,  $\mathbf{r}_1$  and  $\mathbf{r}_2$  are the inner coordinates of nucleus 1 and 2, respectively;  $\mathbf{s} = \mathbf{r} - \mathbf{r}_1 + \mathbf{r}_2$  is the relative coordinate between any given pair of points in the projectile and target, and  $\rho_{1,2}^i$  (with  $i = n, p$ ) are the neutron and proton density distributions.

The exchange part of the potential accounts for the fact that, being identical, the nucleons of the projectile and the target cannot be distinguished from one another

$$V_{\text{Ex}}(r, E_{\text{cm}}) = \sum_{i,j=n,p} \iint \rho_1^i(\mathbf{r}_1, \mathbf{r}_1 + \mathbf{s}) v_{\text{Ex}}^{ij}(\mathbf{s}) \times \rho_2^j(\mathbf{r}_2, \mathbf{r}_2 - \mathbf{s}) \exp \left[ \frac{i\mathbf{k}(r) \cdot \mathbf{s}}{\mu/m_N} \right] d^3\mathbf{r}_1 d^3\mathbf{r}_2, \quad (2)$$

where  $\mu$  is the reduced mass of the colliding system,  $v_{\text{Ex}} = -P_{12}v$  is the exchange contribution from the  $NN$  potential, and the integral runs over the density matrices  $\rho_{1,2}^i(\mathbf{r}, \mathbf{r} \pm \mathbf{s})$  of the nuclei. In this channel, the additional phase renders the double-folding potential dependent on the energy  $E_{\text{cm}}$  in the center-of-mass reference

frame. The momentum for the nucleus-nucleus relative motion  $\mathbf{k}$  is related to  $E_{\text{cm}}$ , the nuclear part of the double-folding potential, and the double-folding Coulomb potential  $V_{\text{Coul}}$  through

$$k^2(r) = \frac{2\mu}{\hbar^2} \left[ E_{\text{cm}} - V_F(r, E_{\text{cm}}) - V_{\text{Coul}}(r) \right]. \quad (3)$$

The density matrices entering in Eq. (2) are approximated using the density matrix expansion (DME) restricted to its leading term [35, 36]. To describe the nuclear density profiles, we use densities inferred from precise electron-scattering measurements [18], and from state-of-the-art nuclear-structure calculations, such as quantum Monte Carlo (QMC) for  $^4\text{He}$  [37] or relativistic mean field (RMF) for heavier nuclei [38].

For the  $NN$  interaction  $v$ , we consider the potentials developed within chiral EFT in Ref. [14], since they give the advantage to work in coordinate space. These potentials are regulated with cutoffs  $R_0 = 1.2$  and  $1.6$  fm, and are based on the formalism developed in Refs. [16, 17]. We will show only results at  $N^2\text{LO}$ , which is the highest order in the chiral expansion in which these potentials are available. We include only two-body forces, leaving the analysis of the impact of three-body interactions for a later study.

### B. Imaginary part: dispersion relations

Between composite projectiles, a simple way to account for excitation and other inelastic processes is to consider complex potentials, known as optical potentials [39]. A general optical potential can be written as a sum of a real term independent of the energy, and a real and an imaginary terms dependent on the energy:

$$U_F(r, E_{\text{cm}}) = V_D(r) + V_{\text{Ex}}(r, E_{\text{cm}}) + iW(r, E_{\text{cm}}), \quad (4)$$

The resulting double-folding potential sum of Eqs. (1) and (2) is purely real. To determine the imaginary part, a simple zeroth order assumption is to consider it proportional to the real double-folding potential:  $W = N_W V_F$  [10], where  $N_W$  is a proportionality constant that in our previous works [14, 15] was taken in the range 0.6–0.8. We have observed a much better agreement with data when dispersion relations are used to construct  $W$  from the real part of the folding interaction [15, 40]. These relations link the energy-dependent real part of an optical potential with its imaginary part. If we can write the local complex optical potential  $U$  between two nuclei as Eq. (4), then its imaginary part can be calculated through [19, 20]:

$$W(r, E_{\text{cm}}) = \frac{1}{\pi} \mathcal{P} \int_{-\infty}^{+\infty} \frac{V_{\text{Ex}}(r, E)}{E - E_{\text{cm}}} dE, \quad (5)$$

where  $\mathcal{P}$  represents the principal value integral.

### III. ${}^4\text{He}$ - ${}^4\text{He}$ ELASTIC SCATTERING

#### A. ${}^4\text{He}$ - ${}^4\text{He}$ potential

To start this study, we analyze the elastic scattering of the symmetric system  ${}^4\text{He}$ - ${}^4\text{He}$  at two laboratory energies: 198.8 and 280 MeV, which correspond to the experimental conditions of Refs. [24–26]. We assess the impact of the density profile as well as the way the imaginary part is determined upon the elastic-scattering cross sections.

Since  ${}^4\text{He}$  is a light and stable nucleus with an equal number of protons and neutrons, we make the approximation  $\rho^p = \rho^n$ . To describe the proton density, we consider three possibilities: a charge density obtained through electron scattering and parametrised as a sum of Gaussians in Ref. [18] (denoted as  $\text{SG}_{\text{ch}}$ ); the corresponding nucleonic density, obtained through the numerical inverse Fourier transform of the Fourier transformed  $\text{SG}_{\text{ch}}$  divided by the nucleonic form factor [41, 42] (named  $\text{SG}_p$ ); and finally, we also use a proton density profile computed within the Quantum Monte Carlo framework (QMC) with two- and three-body local chiral interactions at  $\text{N}^2\text{LO}$  with cutoff  $R_0 = 1.2$  fm [17, 37]. The two-body part of this interaction is the same as the one we use for the calculation of the nucleus-nucleus potentials. These density profiles can be seen in Fig. 1:  $\text{SG}_{\text{ch}}$  in red,  $\text{SG}_p$  in blue, and QMC in green. The  $\text{SG}_p$  and QMC density profiles have a similar shape up to  $r \approx 3$  fm, while  $\text{SG}_{\text{ch}}$  has a more diffuse behavior: a density lower inside the nucleus, and higher at its surface (in the region  $2 \text{ fm} \lesssim r \lesssim 5 \text{ fm}$ ). The unrealistic behavior of  $\text{SG}_{\text{ch}}$  at large distance is due to the nature of the parametrisation.

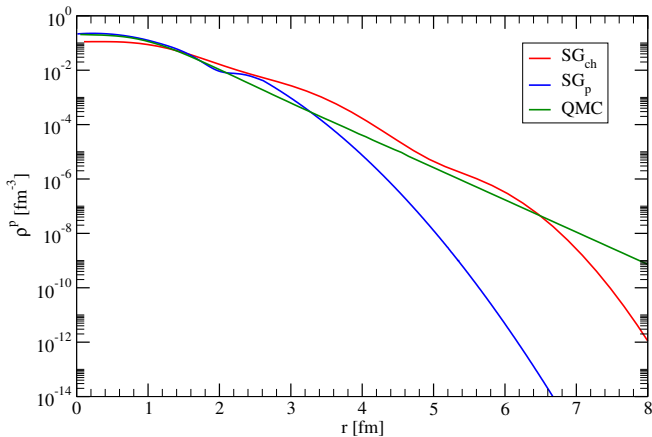


FIG. 1. Proton density profiles for  ${}^4\text{He}$ : the Sum-of-Gaussians charge density derived from electron scattering [18] ( $\text{SG}_{\text{ch}}$ , red), the corresponding proton particle density ( $\text{SG}_p$ , blue), and the density calculated using QMC with local  $\text{N}^2\text{LO}$  potentials [37] (green).

Using the dispersion relations to obtain the imaginary part of the  ${}^4\text{He}$ - ${}^4\text{He}$  potential, we have observed, as in

Ref. [15], that the exchange term (2) shows the same  $r$ -dependence at all energies for all the different  $NN$  interactions and densities considered. Accordingly, we can write in this case:

$$V_{\text{Ex}}(r, E) = f_{\text{Ex}}(r) V_{\text{Ex}}^0(E), \quad (6)$$

and the imaginary part can be calculated as,

$$W(r, E_{\text{cm}}) = \frac{f_{\text{Ex}}(r)}{\pi} \mathcal{P} \int dE \frac{V_{\text{Ex}}^0(E)}{E - E_{\text{cm}}}. \quad (7)$$

The advantage of this expression compared to Eq. (5) is that it suffices to compute the value of the potentials at different energies at one given  $r$ , that we can choose arbitrarily, to obtain the energy dependence and perform the integration (5). This integral requires the depth of  $V_{\text{Ex}}$  at negative energies, that we set as  $V_{\text{Ex}}^0(E < 0) = 0$ . Note that we have tested that setting it to the value of  $V_{\text{Ex}}^0(E = 0)$  instead does not change the results at the energy range of interest in this study.

#### B. Elastic-scattering cross sections

Figure 2 shows the results for elastic scattering-cross sections at  $E_{\alpha} = 198.8$ , and 280 MeV [24–26]. The color code matches that of Fig. 1 for the different density profiles:  $\text{SG}_{\text{ch}}$  in red,  $\text{SG}_p$  in blue, and QMC in green. To illustrate the impact of the  $NN$  cutoff, we show the blue bands, which reflect the  $R_0$  variation between 1.2 and 1.6 fm for the  $\text{SG}_p$  density. For all densities, the solid lines depict the results obtained with dispersive relations. The blue and green curves are close to each other, indicating that the double-folding process probes the densities up to  $r \simeq 3$  fm, since the  $\text{SG}_p$  and QMC profiles in Fig. 2 have different tails but lead to similar cross sections. The cross sections obtained with  $\text{SG}_{\text{ch}}$ , which is the most diffuse density, drop faster with the angle and do not reproduce data as well as the other two, even though this is also a sensible density choice. For all the densities, the dashed lines correspond to cross sections calculated setting  $W = 0.6 V_F$ . These results confirm that dispersive relations give better reproduction of the data, especially at larger angles. This is in agreement with our previous observations [15].

For both energies, the blue band gives very good agreement with experiment and also with the phenomenological optical potentials (POP) from Ref. [24, 26]. These potentials consist of two Woods-Saxon parametrizations with a total of 6 fitted parameters. The increase in the width of the bands reflects the fact that at large angles the short-range  $NN$  physics becomes more relevant. It is important to remember that our results using dispersive relations to determine the imaginary potentials are obtained without any fitting parameter.

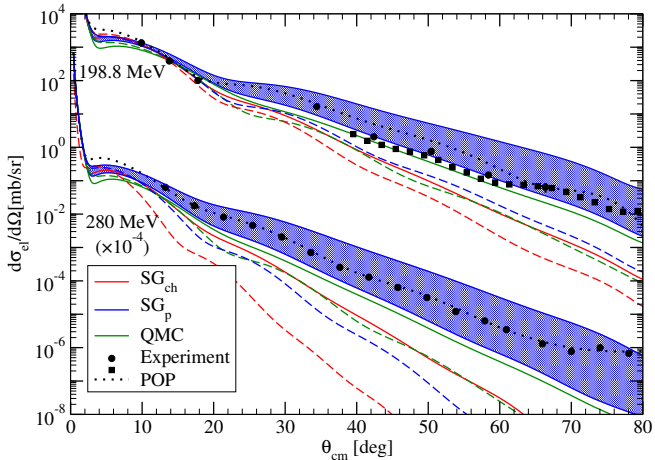


FIG. 2. Elastic scattering cross sections for  $^4\text{He}$ - $^4\text{He}$  at  $E_\alpha = 198.8$ , and  $280$  MeV. The imaginary part is obtained through dispersion relations (solid lines) or considered to be  $W = 0.6 V_F$  (dashed lines). For  $R_0 = 1.2$  fm, results with  $\text{SG}_{\text{ch}}$ ,  $\text{SG}_p$  and QMC are shown in red, blue, and green respectively. For the  $\text{SG}_p$ , the blue band corresponds to a change in  $R_0$  from  $1.2$  fm (lower curve) and  $1.6$  fm (upper curve). POP from Refs. [24, 26] are shown for comparison as black dotted lines. Data from Refs. [24–26].

#### IV. $^4\text{He}$ ELASTIC SCATTERING OFF HEAVIER TARGETS

##### A. Dispersion relations in asymmetric cases

We consider now the elastic scattering of  $^4\text{He}$  with five different targets:  $^{12}\text{C}$ ,  $^{16}\text{O}$ ,  $^{40}\text{Ca}$ ,  $^{48}\text{Ca}$ , and  $^{120}\text{Sn}$  for which we have access to precise nucleonic densities [18, 38] and experimental data sets to which to compare [27–33]. Interestingly, this time the  $r$ -dependence of  $V_{\text{Ex}}$  varies with the collision energy. This is different from what has been seen in Sec. III and in our previous study [15], probably due to the significant asymmetry between the projectile and the target. Therefore, the energy dependence affects both the depth of the potential and its radial shape. To apply dispersion relations, we need to use Eq. (5) and perform the energy integration of the exchange potential at each radial point for all energies. The resulting imaginary part thus exhibits a radial dependence different from that of  $V_{\text{Ex}}$ .

##### B. Scattering on $^{40}\text{Ca}$

Let us first present and detail the results for  $^4\text{He}$ - $^{40}\text{Ca}$  because it best illustrates the issues at hand in these calculations. In this section, we extract conclusions that are valid also for the other systems we will discuss in Sec. IV C. As in Sec. III, we consider  $\text{SG}_{\text{ch}}$ ,  $\text{SG}_p$ , and QMC as density profiles for  $^4\text{He}$ . For  $^{40}\text{Ca}$ , we take the sum-of-Gaussians parametrization of the charge den-

sity inferred from the elastic scattering of electrons from Ref [18] ( $\text{SG}_{\text{ch}}$ ), and the corresponding nucleonic density obtained through the Fourier transform of  $\text{SG}_{\text{ch}}$  divided by the nucleonic form factor ( $\text{SG}_p$ ). In these two cases, we assume the approximation  $\rho^p = \rho^n$ . We consider also a density profile obtained with RMF calculations [38], which provides values for  $\rho^p$  and  $\rho^n$ .

Figure 3 shows the density profiles for  $^{40}\text{Ca}$ . As it was the case for  $^4\text{He}$ ,  $\text{SG}_{\text{ch}}$  (dashed line) gives the most diffuse density profile up to  $r \simeq 7$  fm where the Gaussian parametrization leads to an unrealistic drop. Once again, the  $\text{SG}_p$  and RMF profiles (dashed-dotted and solid lines, respectively) show similar behavior between  $r \approx 1$  fm and  $r \approx 6$  fm for the proton distribution. We show the RMF neutron density as the dotted line. It can be seen that these proton and neutron densities (solid and dotted lines) are close to each other, justifying the approximation assumed for  $\text{SG}_{\text{ch}}$  and  $\text{SG}_p$ .

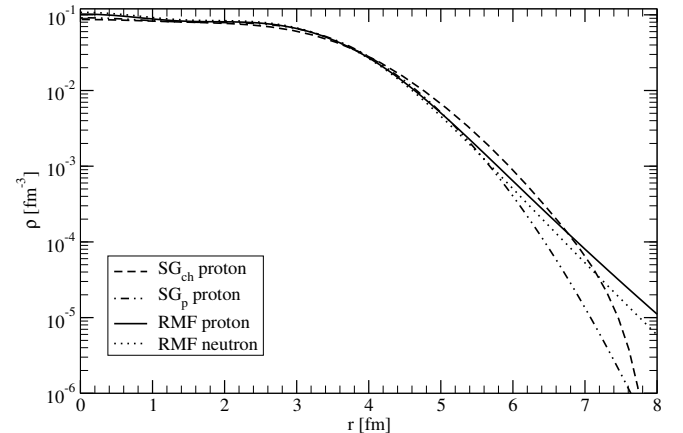


FIG. 3.  $^{40}\text{Ca}$  density profiles: charge density obtained from electron scattering [18] ( $\text{SG}_{\text{ch}}$ , dashed line); the corresponding proton density ( $\text{SG}_p$ , dashed-dotted line), and RMF calculation for protons (solid line) and neutrons (dotted line).

Figure 4 shows elastic-scattering cross sections normalized to Rutherford for  $^4\text{He}$ - $^{40}\text{Ca}$  at  $E_\alpha = 240$  MeV. These results illustrate the sensitivity of our calculations to the choice of the density of both the projectile and the target. In this figure and in the following ones, the labels design the density profiles chosen for  $^4\text{He}$  and the target, in that order. For example, “ $\text{SG}_{\text{ch}}+\text{RMF}$ ” means  $\rho_{^4\text{He}} = \rho_{\text{SG}_{\text{ch}}}$  and  $\rho_{^{40}\text{Ca}} = \rho_{\text{RMF}}$ . All these results are calculated with the  $NN$  cutoff  $R_0 = 1.2$  fm, and the imaginary part is obtained through dispersion relations. Cross sections obtained with  $\rho_{^4\text{He}}$  described as  $\text{SG}_{\text{ch}}$ ,  $\text{SG}_p$  or QMC are shown as red, blue, and green lines, respectively (following the color code of Fig. 1). Results obtained with  $\rho_{^{40}\text{Ca}}$   $\text{SG}_{\text{ch}}$ ,  $\text{SG}_p$  or RMF are shown, respectively, with dashed, dashed-dotted, and solid lines (following the line types in Fig. 3). From this figure, we can conclude that the density of  $^4\text{He}$  has the most significant impact on the results, since the curves are grouped by colors. As

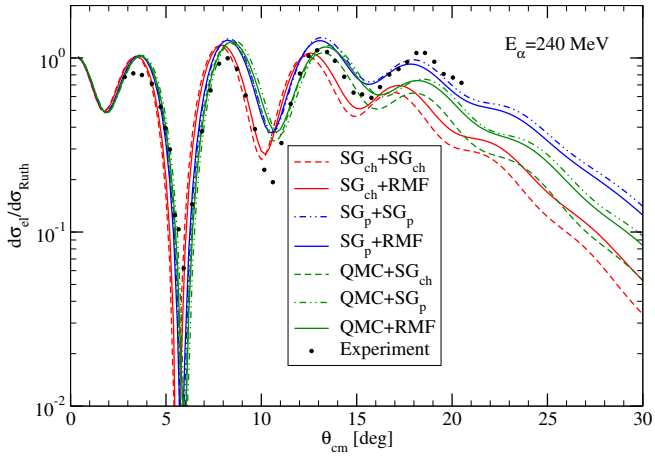


FIG. 4. Elastic-scattering cross sections (normalized to Rutherford) for  ${}^4\text{He}-{}^{40}\text{Ca}$  at  $E_\alpha = 240$  MeV. The potentials are calculated with  $R_0 = 1.2$  fm, and the imaginary part is obtained through dispersion relations. Results obtained with  $\rho_{{}^4\text{He}}$  described as SG<sub>ch</sub>, SG<sub>p</sub> or QMC are shown with red, blue, and green lines, respectively. Results obtained with  $\rho_{{}^{40}\text{Ca}}$  SG<sub>ch</sub>, SG<sub>p</sub> or RMF are shown respectively with dashed, dashed-dotted, and solid lines. Experimental data taken from Ref. [31].

it was seen in the case of  ${}^4\text{He}-{}^4\text{He}$ , the results obtained with SG<sub>ch</sub> (most diffuse density) are the most forward focussed, even in the first minimum, while results with QMC are shifted towards larger angles, starting from the second minimum. SG<sub>p</sub> gives cross sections that are in phase and show the best agreement with experimental data [31]. Nevertheless, it is important to note that using this  $NN$  interaction no density choice enables us to correctly reproduce the second minimum in the data.

As it was the case in  ${}^4\text{He}-{}^4\text{He}$  scattering, we observe that dispersive relations are necessary to reproduce data at large angles. We want to remind the reader that in the calculation of these cross sections there is no parameter fitting. Dispersion relations using SG<sub>p</sub> for  ${}^4\text{He}$  overestimate the magnitude of the minima at intermediate angles, but give the right magnitude at large angles and lead to the right oscillatory pattern when compared to data.

Note that we have explored a fourth density profile for  ${}^{40}\text{Ca}$  obtained through Coupled Cluster calculations using  $\text{N}^2\text{LO}_{\text{sat}}$  potentials [43]. These calculations give a similar density profile to the RMF density around the surface area, and lead to practically indistinguishable elastic-scattering cross sections. This shows that such an observable is not sensitive enough to distinguish the differences between precise nuclear-structure calculations of the density.

### C. Results for heavier targets

#### 1. Medium-mass nuclei

We have observed that the behavior seen in Fig. 4 is general for elastic scattering of the form  ${}^4\text{He}(X,X){}^4\text{He}$ , where  $X$  denotes a target heavier than  ${}^4\text{He}$ . Figure 5 shows results for the cross section as a function of the momentum transfer  $q$ , for  ${}^4\text{He}$  impinging on  ${}^{12}\text{C}$ ,  ${}^{16}\text{O}$ ,  ${}^{40}\text{Ca}$ , and  ${}^{48}\text{Ca}$  at (a)  $E_\alpha = 104$  and (b)  $240$  MeV. All the shown cross sections are calculated choosing SG<sub>p</sub> to describe the  ${}^4\text{He}$  density, because, as illustrated in Figs. 2 and 4, it gives best results in general. In the case of the  $Z = N$  targets, we also chose SG<sub>p</sub> [18], while for  ${}^{48}\text{Ca}$  the density is taken to be that from RMF calculations [38]. The shaded bands show the  $R_0$  1.2–1.6 fm dependence of the cross sections obtained using dispersion relations to constrain the imaginary part of the potentials. To further illustrate the validity of our approach, the dashed lines show the cross sections calculated with  $W = 0.6 V_F$ . We also show results obtained with  $\alpha$ -nucleus global optical potentials (GOP) from Ref. [44] (red dotted lines), which have not been fitted to the data sets that are analyzed in this work. Finally, for  ${}^{12}\text{C}$  and  ${}^{16}\text{O}$  at 104 MeV, the black dotted lines depict the cross sections calculated with POP from Ref. [27], which are modeled as a “wine-bottle” potentials. These phenomenological potentials use 6 parameters and are fitted to the corresponding data sets.

The agreement with the data [27–32] is generally good for all targets. At small angles, dispersive relations and the choice  $W = N_W V_F$  give comparably good results. Nevertheless, dispersion relations are necessary to reproduce the large-angle behavior of the data, since the results obtained with  $W = 0.6 V_F$  deviate from experiment for large  $q$ . The sensitivity to  $R_0$  is large for light targets and decreases with the target mass, and, in general, experimental data lies within that uncertainty band. At 104 MeV, our results for  ${}^{12}\text{C}$  and  ${}^{16}\text{O}$  suffer in comparison to those obtained with POP, which were fitted for each system and energy. Compared to the GOP of Ref. [44], our agreement with data is as good or even better in some cases at both energies and for all targets. We want to point out that for  ${}^4\text{He}-{}^{40}\text{Ca}$  at 240 MeV, the cross section corresponding to  $R_0 = 1.6$  fm (lower line) reproduces the second minimum without increasing the uncertainty of our results in the first minimum, which is an indication of the sensitivity of our problem to short-range physics. It is important to note that we show the results for SG<sub>p</sub>+RMF for  ${}^{48}\text{Ca}$  at both energies for consistency, however the best results at  $E_\alpha = 104$  MeV are obtained with SG<sub>ch</sub>+RMF. Since this is an exception to what we have observed in the other cases, we take this to be an accidental result.

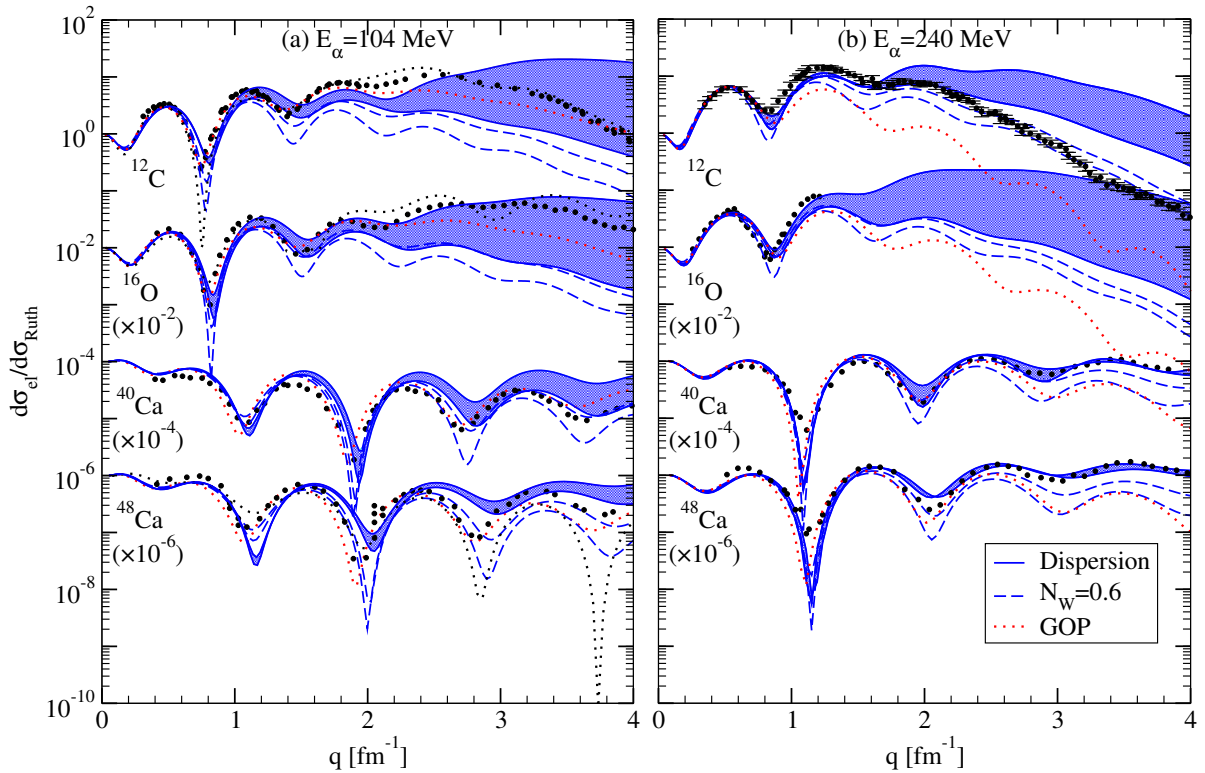


FIG. 5. Elastic scattering cross sections (normalized to Rutherford) as a function of the momentum transfer  $q$  for  ${}^4\text{He}-{}^{12}\text{C}$ ,  ${}^4\text{He}-{}^{16}\text{O}$ ,  ${}^4\text{He}-{}^{40}\text{Ca}$  and  ${}^4\text{He}-{}^{48}\text{Ca}$  at (a)  $E_\alpha = 104$  MeV and (b) 240 MeV. The bands show the  $R_0$  dependence. The imaginary part was obtained through dispersion relations (solid lines) or considered to be  $W = 0.6V_F$  (dashed lines). The chosen densities correspond to the combination that best reproduces experimental data taken from [27, 28], and [29–32]. For comparison, results with POP [27, 31] are shown as black dotted lines. Cross sections obtained with the GOP of Ref. [44] are shown as red dotted lines.

## 2. ${}^{120}\text{Sn}$

Another application of optical potentials generated by double folding can be found in Fig. 6, that displays cross sections for  ${}^4\text{He}-{}^{120}\text{Sn}$  elastic scattering at  $E_\alpha = 386$  MeV [33]. The imaginary part is obtained through dispersion relations (solid lines) or considered to be  $W = 0.6 V_F$  (dashed lines). As for the other targets, we observe a significant sensitivity of our calculations to the choice of the  ${}^4\text{He}$  density, mostly at large angles. Once again, SG<sub>ch</sub> (red lines) leads to cross sections that are shifted towards forward angle, SG<sub>p</sub> (blue lines) produces a cross section mostly in phase with the experimental data [33], and QMC (green lines) is slightly shifted towards larger angles starting at around  $10^\circ$ . However, the magnitude of the cross section is closer to experimental data using the QMC density, and this choice provides the best overall description of the experimental cross section. For this system, we have also tested two more  ${}^{120}\text{Sn}$  densities: a two-parameter Fermi expression [9], and a three-parameter Gaussian [18] profile obtained from electron scattering. We only depict results with RMF densities [38] for  ${}^{120}\text{Sn}$ , since our observations using the other profiles have shown that the choice of this density has

little influence on the cross sections.

Figure 7 explores the  $R_0$  dependence of the cross sections using the density combination QMC+RMF. The green band gives the  $R_0 = 1.2\text{--}1.6$  fm sensitivity when using dispersion relations to calculate the imaginary part (dashed lines show this sensitivity applying the approximation  $W = 0.6 V_F$ ). At large angles, the oscillatory pattern is better reproduced by the dispersion relations, even though the results are similar in magnitude. Note that, in this case, setting  $N_W = 0.8$  (as explored in our previous works [14, 15]) would give a better description of the data. This need for more absorption is probably due to the lower excitation energy of  ${}^{120}\text{Sn}$ , compared to the other targets considered here, as well as the higher density of possible excited states of this target that would lead to open channels that our model does not contemplate.

## V. CONCLUSIONS AND OUTLOOK

We have presented the derivation of  $\alpha$ -target optical potentials through the double folding of local chiral EFT  $NN$  potentials [16, 17] over realistic nucleonic densi-

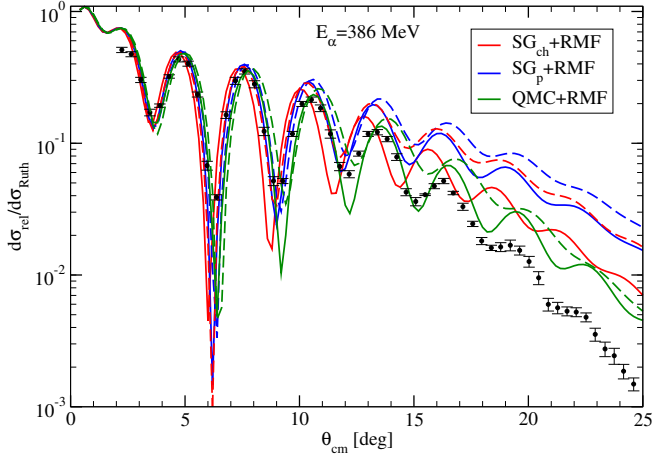


FIG. 6. Elastic-scattering cross sections (normalized to Rutherford) as a function of the center-of-mass angle for  $^4\text{He}$ - $^{120}\text{Sn}$  at  $E_\alpha = 386$  MeV using different  $^4\text{He}$  densities for  $R_0 = 1.2$  fm. The imaginary part is obtained through dispersion relations (solid lines) or considered to be  $W = 0.6 V_F$  (dashed lines). Experimental data from Ref. [33].

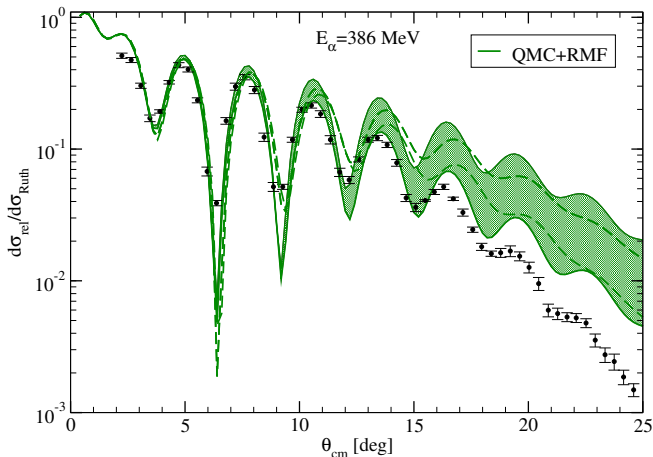


FIG. 7. Same as Fig. 6 exploring the  $R_0$  dependence for QMC+RMF.

ties. To calculate their imaginary part, we have used dispersive relations. The results are potentials generated from first principles without any fitting parameter. Within this framework, we were able to reproduce elastic-scattering data for the collision on  $^4\text{He}$ ,  $^{12}\text{C}$ ,  $^{16}\text{O}$ ,  $^{40}\text{Ca}$ ,  $^{48}\text{Ca}$  and  $^{120}\text{Sn}$  between 100 and 400 MeV.

Dispersion relations lead to a good prediction of data at large angles. This is true for all targets, but especially clear for  $^{12}\text{C}$ , and less good for  $^{120}\text{Sn}$ , target for which our simplified approach might not be sufficient. Contrary to what we have observed in Ref. [15], for asymmetric scat-

tering, the radial shape of the imaginary part is no longer identical to that of the exchange part of the real potential. In these cases, to apply the dispersion relations, the integration over the energy must be performed for each radial point.

We have seen that there are two major inputs for these calculations: the  $\alpha$  density and the  $NN$  interaction. Both of them affect significantly the angular dependence of the cross section. We also have observed that the impact of the target density is less significant for heavier nuclei.

As in our previous work, we find that the use of realistic densities profiles combined with dispersive relations is a necessary first step towards a better description of the imaginary part of nucleus-nucleus potentials, this stays valid for non-symmetric systems and heavy nuclei. There remain several paths for improvement, at the level of both the many-body folding method and the input interactions. First, it would be interesting to study the impact of going beyond leading order in the DME used in Eq. (2). It is also necessary to determine the impact of a calculation beyond Hartree-Fock and the nonlocal contributions that would arise (see, e.g., Refs. [39, 45]). Finally, the role of three-nucleon interactions needs to be investigated in this approach, as they also enter at  $N^2\text{LO}$ . We have observed in preliminary calculations that the contribution to the nucleus-nucleus potential  $^{16}\text{O}$ - $^{16}\text{O}$  arising from three-nucleon interaction is very small compared to the two-body contributions discussed here [46], but the role of these interactions should be investigated in different systems.

Knowing that there is no fitting or scaling parameter in our framework, we can conclude that there is excellent agreement between our calculations of elastic-scattering cross sections and experimental data. These results hint strongly towards the interest of studying the impact of using density profiles based also on chiral EFT interactions to analyse the results within a fully consistent model that would bridge reactions and structure.

## ACKNOWLEDGMENTS

We thank J. Lynn for providing the QMC densities, J. Piekarewicz for the RMF density profiles, and S. Bacca for the Coupled-cluster densities. We also thank the International Atomic Energy Agency that provided the experimental data through their web page [www-nds.iaea.org](http://www-nds.iaea.org). This work was supported by the PRISMA+ (Precision Physics, Fundamental Interactions and Structure of Matter) Cluster of Excellence, the European Union's Horizon 2020 research and innovation programme under Grant Agreement No. 654002, and Deutsche Forschungsgemeinschaft (DFG, German Research Foundation) – Projekt-ID 204404729 – SFB 1044 and Projekt-ID 279384907 – SFB 1245.

---

[1] M. Brandan and G. Satchler, Phys. Rep. **285**, 143 (1997).

[2] M. Vorabbi, P. Finelli, and C. Giusti, Phys. Rev. C **98**, 064602 (2018).

[3] A. Idini, C. Barbieri, and P. Navrátil, .

[4] J. Rotureau, P. Danielewicz, G. Hagen, G. Jansen, F. Nunes, and T. Papenbrock, Springer Proc. Phys. **238**, 183 (2020).

[5] T. Whitehead, Y. Lim, and J. Holt, (2020), arXiv:2009.08436 [nucl-th].

[6] E. Epelbaum, H.-W. Hammer, and U.-G. Meißner, Rev. Mod. Phys. **81**, 1773 (2009).

[7] R. Machleidt and D. R. Entem, Phys. Rep. **503**, 1 (2011).

[8] H.-W. Hammer, A. Nogga, and A. Schwenk, Rev. Mod. Phys. **85**, 197 (2013).

[9] L. C. Chamon, B. V. Carlson, L. R. Gasques, D. Pereira, C. De Conti, M. A. G. Alvarez, M. S. Hussein, M. A. Cândido Ribeiro, E. S. Rossi, Jr., and C. P. Silva, Phys. Rev. C **66**, 014610 (2002).

[10] D. Pereira, J. Lubian, J. R. B. Oliveira, D. P. de Sousa, and L. C. Chamon, Phys. Lett. B **670**, 330 (2009).

[11] T. Furumoto, W. Horiuchi, M. Takashina, Y. Yamamoto, and Y. Sakuragi, Phys. Rev. C **85**, 044607 (2012).

[12] K. Minomo, M. Kohno, and K. Ogata, Phys. Rev. C **93**, 014607 (2016).

[13] D. T. Khoa, N. H. Phuc, D. T. Loan, and B. M. Loc, Phys. Rev. C **94**, 034612 (2016).

[14] V. Durant, P. Capel, L. Huth, A. B. Balantekin, and A. Schwenk, Phys. Lett. B **782**, 668 (2018).

[15] V. Durant, P. Capel, and A. Schwenk, Phys. Rev. C **102**, 014622 (2020).

[16] A. Gezerlis, I. Tews, E. Epelbaum, S. Gandolfi, K. Hebeler, A. Nogga, and A. Schwenk, Phys. Rev. Lett. **111**, 032501 (2013).

[17] A. Gezerlis, I. Tews, E. Epelbaum, M. Freunek, S. Gandolfi, K. Hebeler, A. Nogga, and A. Schwenk, Phys. Rev. C **90**, 054323 (2014).

[18] H. D. Vries, C. D. Jager, and C. D. Vries, At. Data Nucl. Data Tables **36**, 495 (1987).

[19] R. V. Carlson, T. Frederico, M. S. Hussein, H. Esbensen, and S. Landowne, IFUSP/P-802 (1989).

[20] M. M. González and M. E. Brandan, Nuc. Phys. A **693**, 603 (2001).

[21] R. E. Brown and Y. Tang, Nuclear Physics A **170**, 225 (1971).

[22] V. Kukulin, V. Neudatchin, and Y. Smirnov, Nucl. Phys. A **245**, 429 (1975).

[23] A. Al-Ghamdi, A. A. Ibraheem, and M. El-Azab Farid, Int. J. Mod. Phys. E **24**, 1550003 (2015).

[24] L. Woo, K. Kwiatkowski, S. Zhou, and V. Viola, Phys. Rev. C **32**, 706 (1985).

[25] A. Cowley, G. Steyn, S. Fortsch, J. Lawrie, J. Pilcher, F. Smit, and D. Whittal, Phys. Rev. C **50**, 2449 (1994).

[26] K. A. G. Rao, A. Nadasen, D. Sisan, W. Yuhasz, D. Mercer, S. M. Austin, P. G. Roos, and R. E. Warner, Phys. Rev. C **62**, 014607 (2000).

[27] G. Hauser, R. Löhken, H. Rebel, G. Schatz, G. Schweimer, and J. Specht, Nucl. Phys. A **128**, 81 (1969).

[28] H. Gils, E. Friedman, H. Rebel, J. Buschmann, S. Zagromski, H. Klewe-Nebenius, B. Neumann, R. Pesl, and G. Bechtold, Phys. Rev. C **21**, 1239 (1980).

[29] B. John, Y. Tokimoto, Y.-W. Lui, H. L. Clark, X. Chen, and D. H. Youngblood, Phys. Rev. C **68**, 014305 (2003).

[30] Y.-W. Lui, H. L. Clark, and D. H. Youngblood, Phys. Rev. C **64**, 064308 (2001).

[31] D. Youngblood, Y.-W. Lui, and H. Clark, Phys. Rev. C **55**, 2811 (1997).

[32] Y.-W. Lui, D. Youngblood, S. Shlomo, X. Chen, Y. Tokimoto, Krishchayan, M. Anders, and J. Button, Phys. Rev. C **83**, 044327 (2011).

[33] T. Li, U. Garg, Y. Liu, R. Marks, B. Nayak, P. V. M. Rao, M. Fujiwara, H. Hashimoto, K. Nakanishi, S. Okumura, *et al.*, Phys. Rev. C **81**, 034309 (2010).

[34] G. Satchler and W. Love, Phys. Rep. **55**, 183 (1979).

[35] J. W. Negele and D. Vautherin, Phys. Rev. C **5**, 1472 (1972).

[36] S. K. Bogner, R. J. Furnstahl, and L. Platter, Eur. Phys. J. A **39**, 219 (2009).

[37] J. E. Lynn, I. Tews, J. Carlson, S. Gandolfi, A. Gezerlis, K. E. Schmidt, and A. Schwenk, Phys. Rev. C **96**, 054007 (2017).

[38] W.-C. Chen and J. Piekarewicz, Phys. Rev. Lett. **115**, 161101 (2015).

[39] H. Feshbach, Ann. Phys. **5**, 357 (1958).

[40] H. Feshbach, *Theoretical Nuclear Physics* (John Wiley & Sons, Inc., New York, 1992).

[41] P. J. Mohr, D. B. Newell, and B. N. Taylor, .

[42] D. Papoulias and T. Kosmas, Adv. High Energy Phys. **2015**, 763648 (2015).

[43] G. Hagen *et al.*, Nature Phys. **12**, 186 (2016).

[44] M. Nolte, H. Machner, and J. Bojowald, Phys. Rev. C **36**, 1312 (1987).

[45] H. Feshbach, Ann. Phys. **19**, 287 (1962).

[46] S. Weber, *Three-body forces and nucleus-nucleus interactions*, B.Sc. Thesis, Technische Universität Darmstadt (2018).